# Following structural changes in iridium nanoparticles during oxygen evolution electrocatalysis with *operando* X-ray total scattering

Rebecca K. Pittkowski[1,*], Stefanie Punke[1], Andy S. Anker[1], Aline Bornet[2], Nicolas Magnard[1], Nicolas Schlegel[2], Jacob J. K. Kirkensgaard[3,4], Marta Mirolo[5], Jakub Drnec[5], Matthias Arenz[2,*], Kirsten M. Ø. Jensen[1,*]

[1] Department of Chemistry, University of Copenhagen, Universitetsparken 5, 2100 Copenhagen, Denmark

[2] Department of Chemistry, Biochemistry and Pharmaceutical Sciences, University of Bern, Freiestrasse 3, 3012 Bern, Switzerland

[3] Niels Bohr Institute, University of Copenhagen, Universitetsparken 5, 2100 Copenhagen, Denmark

[4] Department of Food Science, University of Copenhagen, Rolighedsvej 26, 1958 Frederiksberg, Denmark

[5] ESRF - The European Synchrotron, 71 Avenue des Martyrs, 38000 Grenoble, France

*corresponding authors: rebecca.pittkowski@chem.ku.dk, matthias.arenz@unibe.ch, kirsten@chem.ku.dk

## Abstract

Understanding the structure of nanoparticles under (electro)catalytic operating conditions is crucial for uncovering structure-property relationships. By combining *operando* X-ray total scattering and PDF analysis with *operando* small-angle X-ray scattering, we obtain comprehensive structural information on ultra-small (< 3 nm) iridium nanoparticles and track their changes during the acidic oxygen evolution reaction. When subjected to electrochemical conditions at reducing potentials, the metallic Ir nanoparticles are found to be decahedral clusters. Upon electrochemical oxidation, iridium oxide forms, containing small rutile-like clusters composed of edge- and corner-connected [$IrO_6$] octahedra of very confined range. These rutile domains are smaller than 1 nm. Combined with SAXS analysis of the particle size, we find that the iridium oxide phase active in the oxygen evolution reaction (OER) lacks crystalline order.

## Introduction

Water electrolysis for hydrogen production is a key technology in the storage of intermittent renewable electricity.[1] Proton exchange membrane (PEM) electrolyzers offer the highest potential for large-scale hydrogen production due to their high efficiency and operational safety, functioning at high pressures and current densities.[1,2] Currently, iridium-based electrocatalysts remain the only viable anode catalysts for PEM electrolyzers, providing excellent stability and activity in the acidic oxygen evolution reaction (OER).[3–5] However, iridium is a very limited resource as one of the scarcest elements on Earth[6]. Therefore, it is crucial to significantly reduce the catalyst loading (in $g_{Ir}$ $kW^{-1}$) to enable large-scale implementation of PEM electrolyzers using iridium catalysts.[6] To fully exploit the iridium used as a catalyst, a high dispersion (surface-to-mass ratio) is essential, and ultra-small iridium nanoparticles (NPs) spread on a high surface area support material provide such a catalyst with high dispersion.[7] So far, it has been established that electrochemically formed

1

iridium oxides that are poorly-crystalline/amorphous outperform crystalline rutile oxides of Ir.[8–11] Moreover, the crystal structure and oxidation state[12] of the iridium oxide plays an important role in catalyst activity and stability.[13,14] However, determining the atomic structure of the electrochemically formed iridium oxide from ultrasmall iridium nanoparticles in the reaction environment remains challenging, meaning that structure/property relations are still not well understood.

It is widely acknowledged that the structure of most synthesized materials should be considered as pre-catalysts rather than the actual catalyst phase, which only forms in the electrochemical environment under reaction conditions.[15,16] In oxygen evolution catalysis, for example, the oxidative potential that is required to drive the conversion of water to oxygen often also leads to redox processes in the catalyst material. Therefore, merely characterizing the as-synthesized catalysts is rarely sufficient.[17,18] To conduct any theoretical, mechanistic studies of the oxygen evolution reaction on a specific catalyst material, it is vital to identify the structural motif forming the catalytically active site.[8,13] As a consequence, numerous *operando* studies of iridium-based electrocatalysts have been conducted to elucidate the catalyst structure under operating conditions. These studies have mostly been focused on different spectroscopic techniques[19] including Raman spectroscopy,[20–24] X-ray photoelectron spectroscopy (XPS),[25–28] and X-ray absorption spectroscopy (XAS).[3,20,29,30] These studies have shown that the oxidation state of iridium is crucial for the OER activity. Changes in oxidation state need to be accompanied by changes in the atomic structure. For ultra-small NPs, it is however difficult to study these changes. While XRD is the most suitable technique to study transformations of crystalline materials in electrochemical environments,[16,31] it does not provide information for ultra-small iridium NPs. Raman and XPS do not provide structural information and XAS analysis is restricted to the first coordination shell. We here apply *operando* X-ray total scattering with pair distribution function (PDF) analysis combined with small-angle X-ray scattering (SAXS) to unravel the structural changes of iridium in the electrochemical environment.

With SAXS it is possible to determine the particle size and morphology of catalyst particles, for example, showing particle agglomeration and atomic rearrangements as previously reported in *in situ* and *operando* SAXS studies of platinum fuel cell catalysts[32–35] and iridium OER catalysts[3] in electrochemical cells. While SAXS gives information on the nanoscale morphology, information on atomic structure is, nevertheless, still missing. Here, PDF analysis can be applied. PDF is now a well-established technique for investigating the atomic structure of amorphous,[36–38] disordered,[39–41] and nanostructured materials.[41–45] Compared to conventional XRD, where only Bragg peaks are considered in the data analysis, total scattering techniques take diffuse scattering into account, which makes it possible to extract structural information of materials with only local structural order. The PDF is the Fourier transform of total scattering data and represents a histogram of interatomic distances in the sample. It is thus an intuitive method for the analysis of scattering data. PDF analysis has been used to study catalyst materials under reaction conditions in e.g. heterogeneous thermal catalysis[46–49] as well as electrochemical transformations of battery materials.[50–52] In the field of electrocatalysis, however, research using X-ray total scattering combined with PDF analysis of catalyst materials under reaction conditions remains scarce: a PEM fuel cell optimized for X-ray total scattering has been developed and used to study alloyed nanoparticles as fuel cell catalysts.[53–55] Despite its relevance for studies of nanocrystalline materials such as Ir nanoparticles, to the best of our knowledge, there have been no reported X-ray total scattering *operando* studies conducted on ultrasmall NPs functioning as electrocatalysts in liquid electrolyte electrochemical cells.

2

In this work, we investigate the structural changes of ultra-small Ir NPs in an electrochemical environment using X-ray total scattering with PDF analysis combined with SAXS. We investigate the atomic structure of the electrochemically formed iridium oxide in acid media under applied oxidative potentials and track the structural modifications during oxygen evolution electrocatalysis. Our results show that the nanoparticle oxidation results in rutile-structured iridium oxides of <1 nm domain size with an increase in particle size during oxidation. An extensively disordered iridium oxide exhibiting only local structure is identified as the OER active phase, highlighting the need for structural studies of electrocatalysts under operating conditions.

## Results and Discussion

### *Electrochemical protocol and operando PDF overview*

Ultra-small iridium nanoparticles were prepared by a colloidal surfactant-free synthesis approach[7,56,57] and immobilized on a high surface area carbon support.[7] Carbon was selected as the support material to maintain dispersion while minimizing any particle-support interactions.[7,58] Electrodes were prepared by vacuum filtration of the Ir/C particles onto a gas diffusion layer to obtain circa 10 micrometer-thick catalyst layers. All experiments were performed in a three-electrode electrochemical cell[59] that allows for collecting X-ray scattering data during the electrochemical experiments. Details on the catalyst, electrode preparation, and *operando* scattering experiments are given in Section 1 – Materials and Methods of the Supporting Information (SI)

X-ray total scattering data were collected at a row of subsequentially applied electrochemical potential steps as shown in Figure 1. Starting from the open circuit potential at circa 0.8 V vs RHE, we first apply a low electrode potential to reduce any oxide that has formed due to exposure to air.[58] Subsequently, the obtained metallic iridium nanoparticles are oxidized at increasingly positive potentials. We apply steps of more and more oxidative potentials up to a point where a significant OER current is measured. In this way, we proceed from metallic iridium to iridium oxidation and into the oxygen evolution regime. The mass activity derived from currents recorded during the potential holds is shown as a function of applied potential in Figure 1 a. By collecting X-ray total scattering data during the electrochemical protocol combined with PDF analysis, we can follow the changes in the atomic structure of the nanoparticles at the respective applied potentials. The overview in Figure 1 b shows the PDFs extracted at each potential step. Peaks in the PDF represent interatomic distances in the material. In all stages of the experiment, PDF peaks are only visible up to around 10 Å, which agrees with the small, nanoscale nature of the prepared particles.[7,56]

The PDF peak at ca. 2 Å, highlighted in light red in the right panel in Figure 1 b, corresponds to the first Ir-O distance. By analyzing the intensity of this peak, we can follow the oxide content in the nanoparticle structure. At open circuit potential, the particles are partially oxidized and the Ir-O peak is visible, as seen from the PDF plotted in gray in Figure 1 b. Once a low electrode potential is applied (0.2 V vs RHE), a reductive current is recorded (see Fig. 1 a and SI, Fig. S4) indicating the reduction of the nanoparticles to metallic iridium. The characteristic distances in the PDF of the metallic particles (blue PDFs in Fig. 1 b) differ significantly from the oxidized particles and the Ir-O peak disappears. Instead, a strong Ir-Ir peak (2.7 Å) from the metal dominates the PDF, which is highlighted in light blue in Figure 1 b.
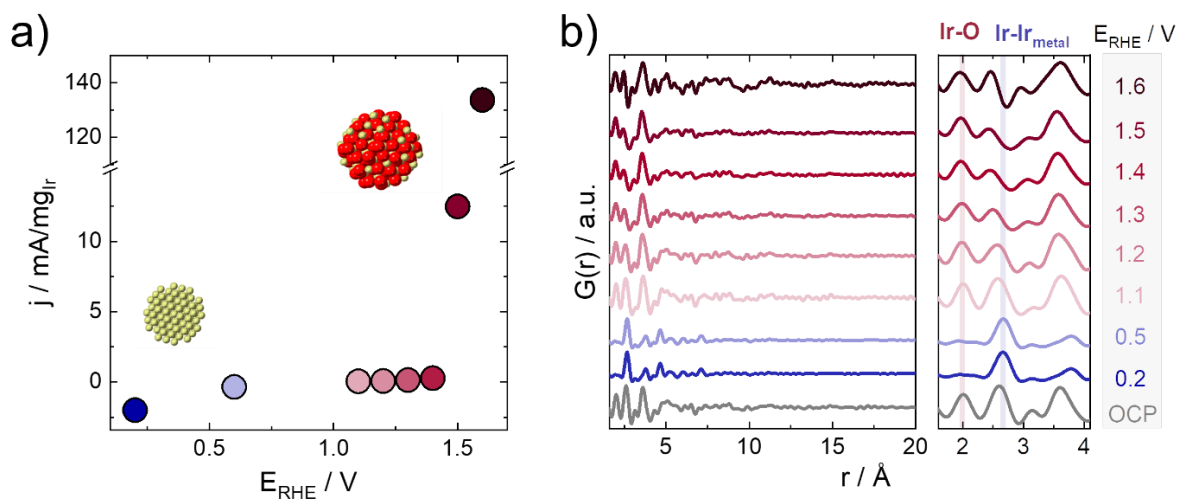
3

Figure 1: a) Mass activity derived from the currents collected during 10 min potential holds (chronoamperometry), currents are averaged over the last 100 seconds, and b) corresponding *operando* PDFs extracted from X-ray total scattering data collected at the respective potentials, with zoom in on the local range of the PDFs in the region 2 to 4 Å. The Ir-O distance from iridium oxide is highlighted in light red and the Ir-Ir metal pair distance in light blue.

We follow the oxidation of the iridium NPs by gradually increasing the electrode potential. At 0.5 V vs RHE, the particles remain metallic. Starting from 1.1 V vs RHE, increasing oxidative currents are recorded for each potential step, corresponding to iridium oxidation as seen in Figure 1 a. At this point, the Ir-O peak reappears in the PDFs, showing the oxide character of the catalyst at the applied potentials. At 1.5 V and 1.6 V vs RHE, significant OER currents are recorded, as shown in Figure 1 a. The corresponding Tafel plots (E vs log j) of the *operando* experiment are included in the SI (Fig. S5) displaying a distinction between the activation and the OER regime in the electrochemical data. The PDFs collected at these potentials thus allow us to extract information on the atomic structure of the active catalyst during oxygen evolution.

To ensure the reproducibility of both the electrochemical performance as well as the structural information obtained, the experiment was repeated for a second catalyst film. The same behavior in the reduction and oxidation of the particles can be followed in the PDFs of the repeat measurement as shown in the Supporting Information, Figures S6-7.

### *Structure of electrochemically reduced Ir nanoparticles*

Having established the overall evolution in atomic structure in the potential steps, we now analyze the PDFs in detail. We first address the structure of the reduced, metallic Ir nanoparticles. The PDF extracted at 0.2 V vs RHE is characteristic of a metallic nanoparticle with pair distances extending to circa 12 Å (see Fig. 2 a). Bulk metallic iridium is known to crystallize in the face-centered cubic (*fcc*) crystal system, and we first test if the nanoparticles adopt the same structure. The extracted PDF can however not be fully described by an *fcc* model, see fit in Figure 2 a ($R_w$ = 0.34). Certain peaks appear in the PDF, e.g., at circa 5 Å (area highlighted in gray in Fig. 2 a), which do not correspond to pair distances in the bulk *fcc* structure.

4

It is well-known that small metallic NPs can differ in structure from their bulk counterparts and take e.g. multi-twinned structures forming e.g. decahedral[60–62] or icosahedral particles.[63] It has furthermore been shown that Os NPs can form both *fcc* and hexagonal close-packed (*hcp*) structures,[64] and in other systems, stacking faults have been seen to be dominating for small nanoparticles.[65] PDF analysis allows us to characterize and distinguish between such structures, as it is sensitive to the local atomic arrangements.[59–61] Recently developed tools allow to automation of the analysis of PDFs from metallic nanoparticles to identify the best-fitting model.[69,70] Here, we first applied our newly developed method, DeepStruc, which uses Machine Learning to solve the structure of monometallic nanoparticles of up to 200 atoms from PDF.[70,71] As seen in Fig. S9, DeepStruc suggests that the metallic Ir nanoparticles take either a *hcp* or a decahedral structure. When fitting a *hcp* cluster model (Figure S8 b), the peak at circa 5 Å is included in the simulated PDF, which was absent when using the *fcc* model. The *hcp* model is, however, also not able to describe all the distances present in the PDF ($R_w = 0.33$). A better fit is achieved with a two-phase model including both an *fcc* and an *hcp* phase ($R_w = 0.28$), which is shown in Figure 2 b. Mixtures of crystalline *hcp* and *fcc* Ir phases under electrochemical reductive conditions have been reported.[72] Also, a two-phase model of *fcc* and *hcp* structures has previously been used for PDF modeling of close-packed structures that contain stacking faults.[65] The agreement between data and the two-phase model could thus indicate that the nanoparticles consist of defective, closed-packed structures. However, the model assumes a spherical shape factor, and the crystallite sizes refine to 9 Å for the *fcc* and 11 Å for the *hcp* phase. Therefore, to further analyze the NP structure, their particle size was analyzed with SAXS as well. We obtain a mean particle size of 14 Å by fitting a model of polydisperse spherical particles with a lognormal distribution (polydispersity of PD = 0.2) and a power-law to the SAXS curve as shown in Figure 2 d and Table S1. The log-normal size distribution of the polydisperse spheres model fit to the SAXS data is presented in Figure 2 e. The SAXS results thus do not agree with the two-phase *fcc* and *hcp* model.

We now consider decahedral structures, which were also suggested by DeepStruc. Decahedral particles are constructed from *fcc*-shaped crystals separated by twin boundaries, resembling stacking faults.[70] Decahedral metal nanoparticles are readily obtained in many systems,[73] and the formation of decahedral Ir nanoparticles has been reported via a similar synthesis route.[74] To validate our modeling approach further, we used a brute-force structure-mining algorithm[69,70] as presented in the SI in Table S2 and Figure S10. This algorithm also suggests decahedral particles as best-fitting structural models, and the best fit when modeling the experimental PDF with an $Ir_{192}$ decahedral particle (Figure 2 f). The fit result is presented in Figure 2 c ($R_w = 0.31$). Compared to the two-phase *fcc*/*hcp* model, the decahedral $Ir_{192}$ cluster has a diameter (ca. 16 Å) that agrees better with the particle diameter obtained in the SAXS measurement, while the fit obtains a comparable $R_w$ value and uses significantly fewer parameters in the fitting procedure

The match between the PDF and SAXS size analyses is highlighted when comparing the diameters obtained from the PDF fits for the different structural models to the particle size distributions obtained from the SAXS model, as shown in Figure 2 e. It can be expected that the data can be even better described by introducing a distribution of differently sized decahedral particles or additional stacking faults in the metallic nanoparticles.
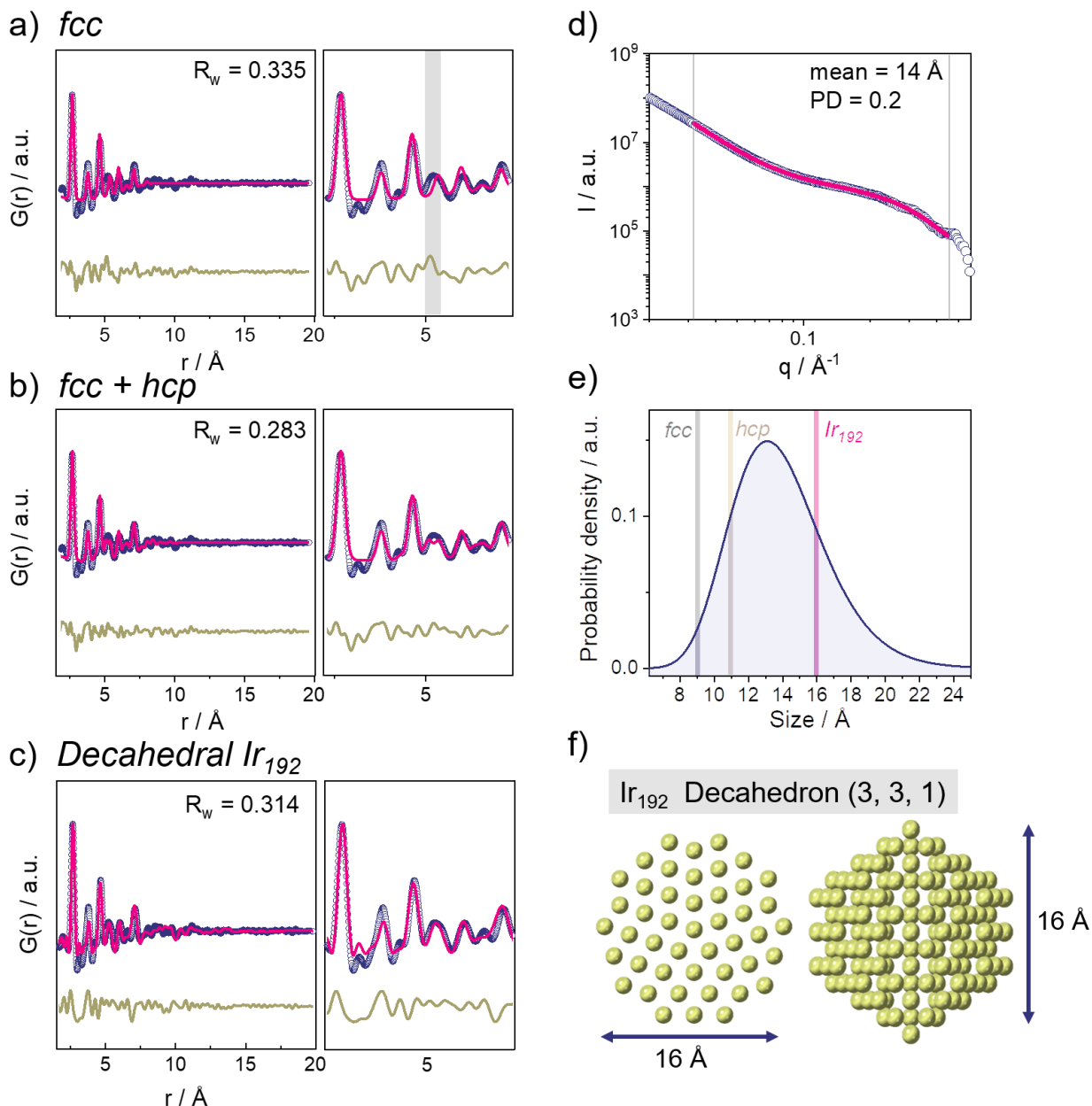
5

Figure 2: Characterization of metallic nanoparticles obtained through electrochemical reduction (potential hold at 0.2 V vs RHE) with a) fit of an *fcc* phase model, b) two-phase model with both an *fcc* and *hcp* phase to the PDF and c) best fit of a model of decahedral particles to the PDF: the decahedral particle is constructed with three layers parallel to the fivefold axis, three layers truncated perpendicular to the pentagonal edges and one layer truncated perpendicular to the five apical vertices (192 Ir atoms). Figure d) shows the fit to the SAXS data of a model of polydisperse spherical particles, as well as e) as probability density of the log-normal size distribution with added particle diameters obtained from the different PDF structural models and f) structure of the $Ir_{192}$ decahedral cluster.

6

*Electrochemical formation of iridium oxide before OER*

We now analyze the oxide formation under electrochemical conditions in detail. From a potential of 1.1 V vs RHE, oxide formation is evident in the Ir catalyst. The local range of the PDF obtained at this potential is shown in Figure 3 a. In the PDF the Ir-O peak at circa 2 Å - highlighted in red - evidences the oxidic character of the material. Further peaks are seen at ca. 3.2 Å and 3.6 Å, highlighted in orange and brown in Figure 3 a. These peaks agree well with Ir-Ir distances in iridium oxide. Based on reported crystalline iridium oxide structures,[75,76] we can assign the peak at ca. 3.2 Å to Ir-Ir in neighboring edge-sharing [IrO$_6$] octahedra (orange arrow in the structure cut-out), while the one at 3.6 Å corresponds to Ir-Ir in corner-sharing [IrO$_6$] octahedra (brown arrow in the structure cut-out). Simulated PDFs of different iridium oxides are presented in Figure S11. Based on the ratio of corner-sharing to edge-sharing Ir octahedra, we can further characterize the atomic structure of the formed iridium oxide. Hollandite-type iridium oxide motifs, which have been found in low-crystalline iridium oxide samples that are highly OER active,[75] would be characterized by an equal number of corner-sharing to edge-sharing [IrO$_6$] octahedral units. As seen in Figure S11, this leads to two Ir-Ir peaks of similar intensity. However, in our experimental PDF, the corner-sharing peak is more intense than the edge-sharing peak. This ratio of corner-sharing and edge-sharing Ir octahedra indicates the presence of a rutile-type oxide, where one [IrO$_6$] octahedron has two and eight edge-and corner-sharing neighbors, respectively, see structure cut-out in Figure 3.

The PDF contains very few peaks at distances larger than 4 Å. This indicates a very disordered oxide with a rutile-type local motif of edge- and corner-sharing [IrO$_6$] structural units. The PDF also shows that at 1.1 V vs RHE, the iridium metal is not completely oxidized, as the edge-sharing Ir-Ir distance of circa 2.7 Å (blue highlight in Figure 3 a) is still visible. When compared to the partially oxidized particles in the catalyst film at open circuit potential, we find no significant differences in the iridium oxide structure formed at 1.1 V vs RHE, as can be seen in Figure 1.

We note here that the Ir-Ir distances in the oxide phase are slightly larger than those previously observed from *operando* extended x-ray absorption fine structure (EXAFS).[29] This relates to the *operando* PDF data treatment. Before Fourier-transforming the total scattering data to obtain the PDF, the signal from the carbon support is subtracted to isolate only the contribution from the catalyst. Despite our efforts, achieving a complete background correction of the carbon support proved difficult for the *operando* measurements. This difficulty is mainly related to the fact that the carbon support changes during the measurement, i.e., it becomes oxidized. We therefore observe an additional peak at around 1.4 Å in the PDF, which corresponds to the C-C distance in the carbon support. The PDF of the carbon support is shown in Figure S12. We note that a second C-C distance from the support is expected at 2.5 Å (Figure S12), which is however hidden underneath the Ir-Ir$_{metal}$ distance. The superposition of the two signals leads to an apparent shift of the Ir-Ir metal distance to smaller distances, which we regard as an artifact from the insufficient background correction of the carbon support. Similarly, the peak originating from the Ir-Ir$_{corner}$ distance is convoluted with the signal from the C-C distance at around 3.7 Å, which can explain why relatively long distances are obtained for this particular peak in the PDF as compared to crystalline iridium [76] and in *operando* EXAFS (both 3.55 Å).[29]
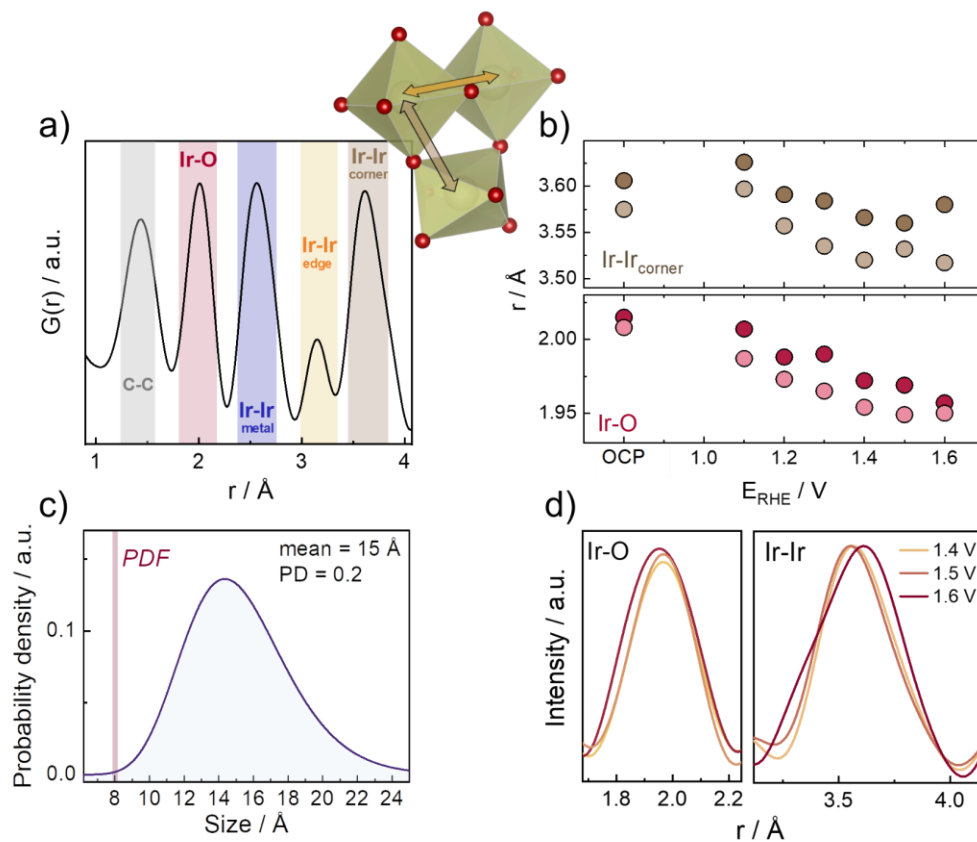
Figure 3: a) Local range (1 - 4 Å) of the PDF of the electrochemically formed iridium oxide with remaining metallic iridium in the particle core (1.1 V vs RHE) and illustration of a rutile structural motif of edge- and corner-sharing [IrO$_6$] octahedral units and b) evolution of Ir-Ir distance of corner-sharing octahedra and Ir-O distance in the iridium oxide as a function of applied potential. A repeated measurement is added (light markers) to confirm the general trends. c) Log-normal size distribution of the SAXS model fit to the 1.5 V vs RHE data, with a mean size of 15 Å and a polydispersity (PD) of 0.2. The diameter of the rutile model fit to the PDF data collected at 1.5 V vs RHE is indicated with the red line marked PDF. d) zoom in on the Ir-O and Ir-Ir pair distances of the PDFs collected at 1.4, 1.5, and 1.6 V vs RHE.

### _Changes in catalyst structure when going to OER conditions_

When we apply increasingly oxidative potential steps, small changes in the atomic structure of the particles can be observed in the PDFs. Figure 3 b (bottom panel) shows the Ir-O distance obtained from the PDFs plotted in Figure 1. The Ir-O distance is plotted as a function of potential, and we note a shift in the Ir-O pair distance to smaller distances. This corresponds to a contraction of the Ir-O bond when iridium becomes progressively more oxidized. This trend has previously been observed in an _operando_ EXAFS study of ultra-small Ir nanoparticles of ca. 2 nm diameter, prepared by the Adams fusion method when applying potential steps in the same potential region.[29] Similarly, the Ir-Ir distance of ca. 3.6 Å in corner-sharing [IrO$_6$] becomes shorter when the potential is increased, indicating a contraction of the iridium oxide structure at higher potentials, which agrees with more oxidized iridium (Figure 3b, upper panel).

8

The same trend is observed for the repeated measurement of a second catalyst film (light markers in Figure 3 b), confirming that this is a general trend. The extracted distances for the two different measurements differ only slightly. The deviations of absolute lattice parameters extracted from the PDFs are likely due to variations in the alignment of the sample when measuring in *operando* conditions, which lead to slight differences in sample-to-detector distance in the different experiments. Therefore, the investigation of trends in the evolution of bond and pair distances is more relevant in this study. We furthermore note here that the observed contraction might in reality be larger than observed here, as it is influenced by a change in the contribution of the carbon signal, and the convolution of the Ir-Ir distance with the C-C signal shifts the observed distance to higher r.

The amount of metal present in the partially oxidized particles is continuously reduced, as can be followed by the shift in the metal Ir-Ir / C-C peak in Figure 1. The peak moves gradually closer to 2.5 Å when the potential is increased from 1.1-1.4 V vs RHE. At this point, the radial distance of the observed peaks agrees with the reference C-C distance, and no further movement in the peaks is observed when applying a potential of 1.5 or 1.6 V vs RHE.

*Structural disorder in the OER active oxide*

No substantial changes in oxide structure are visible at 1.5 and 1.6 V vs RHE, where a significant OER current is measured, as seen in Figure 1 a. Still, the local coordination of a rutile-type oxide with edge and corner-sharing [IrO$_6$] octahedra is evident and no long-range order is visible. At the potential of 1.6 V vs RHE, peak broadening is observed, which can be interpreted as increasing mobility of the atoms in the structure at higher oxygen evolution currents (steady-state current i = 130 mA/mg$_{Ir}$).

To highlight the disordered nature of the electrochemically formed iridium oxide, we compare the sizes extracted for the particles at 1.5 V vs RHE from the SAXS data compared to the corresponding PDF data. Fitting a polydisperse sphere model to the SAXS data (Figure S13), we obtain a mean particle size of 15 Å in diameter. The log-normal size distribution of the particles is shown in Figure 3 c. To estimate the domain size of the identified rutile structure motif, we fit a model of a rutile-type oxide to the *operando* PDF. The results are summarized in Fig. S14. Assuming a spherical shape model, the diameter of the rutile phase in the PDF modeling results in only 8 Å. We note that the PDF still shows small, weak features at larger r-distances, which could be due to several effects, such as particle size distribution, structural disorder, or amorphous shell formation. However, the much smaller spherical diameter of the iridium oxide obtained from the PDF (highlighted in red in Figure 3 c) compared to the SAXS model indicates a very disordered iridium oxide shell at larger r-distances. An increase in structural variability with more oxidative potential is further reflected in the peak broadening of the Ir-O and Ir-O pair distances observed in the PDFs at 1.6 V vs RHE, which are presented in zoom-in in Figure 3 d. This is also evident from the increasing atomic displacement parameters U$_{iso}$, of both Ir and O, obtained from the rutile structural model that we fit to the *operando* PDF data. At 1.4 V vs RHE, an U$_{iso}$ value of 0.006 Å$^2$ for Ir and 0.01 Å$^2$ for O is obtained, while at 1.6 V vs RHE, these are increased to 0.02 Å$^2$ and 0.11 Å$^2$ for Ir and O, respectively. This highlights that under operating conditions, the OER active iridium oxide catalyst is characterized by a large amount of structural disorder.

Only by combining *operando* SAXS and PDF analysis, we can fully characterize the structure of the electrochemically formed OER active oxide. The information that is obtained from the different

9

techniques is sketched in Figure 4. By extracting the nanoparticle size from SAXS and the structural motifs from PDF analysis, we show that the OER-active iridium oxide phase is highly structurally disordered. The oxide consists of Ir-O octahedral units that are connected in a rutile-like fashion in small clusters ordered up to max. 8 Å, while the particle itself is much larger with a 15 Å diameter. Structural flexibility and disorder have been related to higher OER activity, which is e.g. observed in electrochemically prepared iridium oxide when compared to calcined crystalline rutile $IrO_2$.[10]
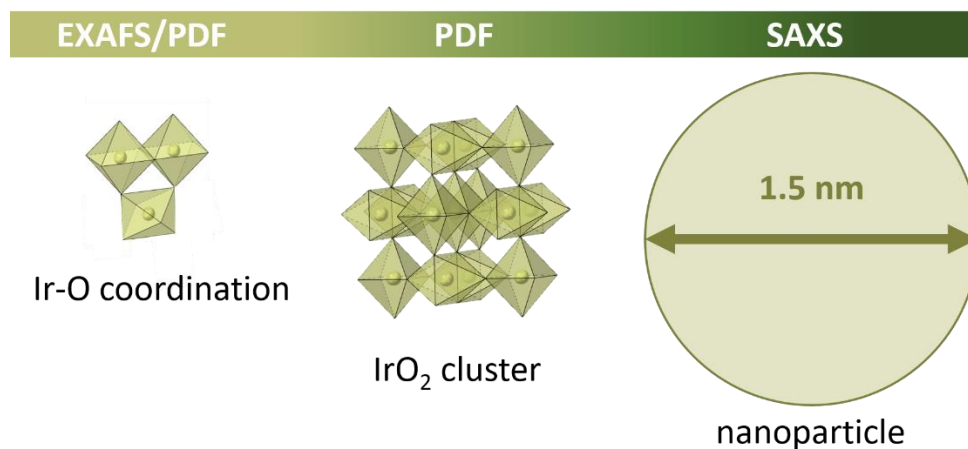


Figure 4: Sketch illustrating the information that can be extracted by *operando* X-ray PDF and SAXS on the structure of the electrochemically formed iridium oxide, which is active in the oxygen evolution reaction. While PDF can provide information on the very local Ir-O and Ir-Ir coordination similar to EXAFS, PDF can also provide information on mid-range structural information of the arrangement of metal polyhedra within the nanoparticle. Combined with morphological information from SAXS, a complete picture of the atomic structural arrangement in the iridium oxide nanoparticle is obtained.

**Conclusions**

We investigate the structural dynamics of ultra-small iridium nanoparticles exposed to an electrocatalytic environment. Employing a combination of *operando* of X-ray total scattering and PDF analysis with analysis of operando SAXS data, we can extract valuable insights into the atomic arrangement and morphology of the Ir nanoparticles under reaction conditions. We first reduce the particles to study the structure of the metallic Ir nanoparticle under potential control, but non-reactive conditions. Interestingly, the atomic structure of the Ir nanoparticles cannot be fully described by an *fcc* phase but shows additional *hcp*-like features. Further analysis of the PDF reveals that the metallic nanoparticles are most likely $Ir_{192}$ decahedral clusters. The diameter of the $Ir_{192}$ cluster is comparable to the mean particle diameter obtained from the SAXS analysis (14 Å). When applying oxidative potentials, we identified a clear formation of a disordered iridium oxide. The local structure of the electrochemically formed oxide contains both corner- and edge-sharing Ir-O octahedra, similar to a rutile oxide, albeit displaying limited structural order. Increasing the applied potential, we observed that the residual metal is gradually oxidized and that the iridium oxide structure contracts. At relevant oxygen evolution current densities, a discernable rise in atomic mobility became evident, notably reflected in large ADP values for Ir and especially O.

https://doi.org/10.26434/chemrxiv-2023-zbtlg-v2 **ORCID:** https://orcid.org/0000-0002-0351-4993 Content not peer-reviewed by ChemRxiv. **License:** CC BY-NC-ND 4.0

Using *operando* SAXS analysis, we determine the diameter of the iridium oxide nanoparticles to be consistently around 15 Å at 1.5 V vs RHE. Given that the PDF only displays atomic pair distances up to 8 Å for iridium oxide, we infer that the atomic structure of the OER-active oxide exhibits considerable disorder, yet contains local rutile-like structural motifs. In conclusion, our findings underscore that *operando* PDF analysis is a powerful tool to extract information on the atomic arrangement of ultra-small nanoparticles. When combined with *operando* SAXS analysis, this approach provides a comprehensive understanding of the disordered nature of the OER active phase that is formed in the electrochemical environment.

## Data availability

The experimental data collected for this manuscript are accessible through the ESRF for proposal CH 6227 via the following doi: 10.15151/ESRF-ES-790330698

## References

(1) Carmo, M.; Fritz, D. L.; Mergel, J.; Stolten, D. A Comprehensive Review on PEM Water Electrolysis. *Int. J. Hydrog. Energy* **2013**, *38* (12), 4901–4934. https://doi.org/10.1016/j.ijhydene.2013.01.151.

(2) Shiva Kumar, S.; Himabindu, V. Hydrogen Production by PEM Water Electrolysis – A Review. *Mater. Sci. Energy Technol.* **2019**, *2* (3), 442–454. https://doi.org/10.1016/j.mset.2019.03.002.

(3) Povia, M.; F. Abbott, D.; Herranz, J.; Heinritz, A.; Lebedev, D.; Kim, B.-J.; Fabbri, E.; Patru, A.; Kohlbrecher, J.; Schäublin, R.; Nachtegaal, M.; Copéret, C.; J. Schmidt, T. Operando X-Ray Characterization of High Surface Area Iridium Oxides to Decouple Their Activity Losses for the Oxygen Evolution Reaction. *Energy Environ. Sci.* **2019**, *12* (10), 3038–3052. https://doi.org/10.1039/C9EE01018A.

(4) She, L.; Zhao, G.; Ma, T.; Chen, J.; Sun, W.; Pan, H. On the Durability of Iridium-Based Electrocatalysts toward the Oxygen Evolution Reaction under Acid Environment. *Adv. Funct. Mater.* **2022**, *32* (5), 2108465. https://doi.org/10.1002/adfm.202108465.

(5) Naito, T.; Shinagawa, T.; Nishimoto, T.; Takanabe, K. Recent Advances in Understanding Oxygen Evolution Reaction Mechanisms over Iridium Oxide. *Inorg. Chem. Front.* **2021**, *8* (11), 2900–2917. https://doi.org/10.1039/D0QI01465F.

(6) Minke, C.; Suermann, M.; Bensmann, B.; Hanke-Rauschenbach, R. Is Iridium Demand a Potential Bottleneck in the Realization of Large-Scale PEM Water Electrolysis? *Int. J. Hydrog. Energy* **2021**, *46* (46), 23581–23590. https://doi.org/10.1016/j.ijhydene.2021.04.174.

(7) Bornet, A.; Pittkowski, R.; Nielsen, T. M.; Berner, E.; Maletzko, A.; Schröder, J.; Quinson, J.; Melke, J.; Jensen, K. M. Ø.; Arenz, M. Influence of Temperature on the Performance of Carbon- and ATO-Supported Oxygen Evolution Reaction Catalysts in a Gas Diffusion Electrode Setup. *ACS Catal.* **2023**, 7568–7577. https://doi.org/10.1021/acscatal.3c01193.

(8) Lee, S.; Lee, Y.-J.; Lee, G.; Soon, A. Activated Chemical Bonds in Nanoporous and Amorphous Iridium Oxides Favor Low Overpotential for Oxygen Evolution Reaction. *Nat. Commun.* **2022**, *13* (1), 3171. https://doi.org/10.1038/s41467-022-30838-y.

(9) Elmaalouf, M.; Odziomek, M.; Duran, S.; Gayrard, M.; Bahri, M.; Tard, C.; Zitolo, A.; Lassalle-Kaiser, B.; Piquemal, J.-Y.; Ersen, O.; Boissière, C.; Sanchez, C.; Giraud, M.; Faustini, M.; Peron, J. The Origin of the High Electrochemical Activity of Pseudo-Amorphous Iridium Oxides. *Nat. Commun.* **2021**, *12* (1), 3935. https://doi.org/10.1038/s41467-021-24181-x.

(10) Saveleva, V. A.; Wang, L.; Teschner, D.; Jones, T.; Gago, A. S.; Friedrich, K. A.; Zafeiratos, S.; Schlögl, R.; Savinova, E. R. Operando Evidence for a Universal Oxygen Evolution Mechanism on Thermal and Electrochemical Iridium Oxides. *J. Phys. Chem. Lett.* **2018**, *9* (11), 3154–3160. https://doi.org/10.1021/acs.jpclett.8b00810.

(11) Pfeifer, V.; Jones, T. E.; Velasco Vélez, J. J.; Massué, C.; Arrigo, R.; Teschner, D.; Girgsdies, F.; Scherzer, M.; Greiner, M. T.; Allan, J.; Hashagen, M.; Weinberg, G.; Piccinin, S.; Hävecker, M.; Knop-Gericke, A.; Schlögl, R. The Electronic Structure of Iridium and Its Oxides. *Surf. Interface Anal.* **2016**, *48* (5), 261–273. https://doi.org/10.1002/sia.5895.

(12) Diklić, N.; Clark, A. H.; Herranz, J.; Aegerter, D.; Diercks, J. S.; Beard, A.; Saveleva, V. A.; Chauhan, P.; Nachtegaal, M.; Huthwelker, T.; Lebedev, D.; Kayser, P.; Alonso, J. A.; Copéret, C.; Schmidt, T. J. Surface Ir+5 Formation as a Universal Prerequisite for O2 Evolution on Ir Oxides. *ACS Catal.* **2023**, *13* (16), 11069–11079. https://doi.org/10.1021/acscatal.3c01448.

(13) Flores, R. A.; Paolucci, C.; Winther, K. T.; Jain, A.; Torres, J. A. G.; Aykol, M.; Montoya, J.; Nørskov, J. K.; Bajdich, M.; Bligaard, T. Active Learning Accelerated Discovery of Stable Iridium Oxide Polymorphs for the Oxygen Evolution Reaction. *Chem. Mater.* **2020**, *32* (13), 5854–5863. https://doi.org/10.1021/acs.chemmater.0c01894.

(14) Sharma, R.; Karlsen, M. A.; Morgen, P.; Chamier, J.; Ravnsbæk, D. B.; Andersen, S. M. Crystalline Disorder, Surface Chemistry, and Their Effects on the Oxygen Evolution Reaction (OER) Activity of Mass-Produced Nanostructured Iridium Oxides. *ACS Appl. Energy Mater.* **2021**, *4* (3), 2552–2562. https://doi.org/10.1021/acsaem.0c03127.

(15) Jiang, H.; He, Q.; Zhang, Y.; Song, L. Structural Self-Reconstruction of Catalysts in Electrocatalysis. *Acc. Chem. Res.* **2018**, *51* (11), 2968–2977. https://doi.org/10.1021/acs.accounts.8b00449.

(16) Zhu, Y.; Kuo, T.-R.; Li, Y.-H.; Qi, M.-Y.; Chen, G.; Wang, J.; Xu, Y.-J.; Ming Chen, H. Emerging Dynamic Structure of Electrocatalysts Unveiled by in Situ X-Ray Diffraction/Absorption Spectroscopy. *Energy Environ. Sci.* **2021**, *14* (4), 1928–1958. https://doi.org/10.1039/D0EE03903A.

(17) Juodkazytė, J.; Šebeka, B.; Valsiunas, I.; Juodkazis, K. Iridium Anodic Oxidation to Ir(III) and Ir(IV) Hydrous Oxides. *Electroanalysis* **2005**, *17* (11), 947–952. https://doi.org/10.1002/elan.200403200.

(18) Kuznetsov, D. A.; Han, B.; Yu, Y.; Rao, R. R.; Hwang, J.; Román-Leshkov, Y.; Shao-Horn, Y. Tuning Redox Transitions via Inductive Effect in Metal Oxides and Complexes, and Implications in Oxygen Electrocatalysis. *Joule* **2018**, *2* (2), 225–244. https://doi.org/10.1016/j.joule.2017.11.014.

(19) Zuo, S.; Wu, Z.-P.; Zhang, H.; Lou, X. W. (David). Operando Monitoring and Deciphering the Structural Evolution in Oxygen Evolution Electrocatalysis. *Adv. Energy Mater.* **2022**, *12* (8), 2103383. https://doi.org/10.1002/aenm.202103383.

(20) Mo, Y.; Stefan, I. C.; Cai, W.-B.; Dong, J.; Carey, P.; Scherson, D. A. In Situ Iridium LIII-Edge X-Ray Absorption and Surface Enhanced Raman Spectroscopy of Electrodeposited Iridium Oxide Films in Aqueous Electrolytes. *J. Phys. Chem. B* **2002**, *106* (14), 3681–3686. https://doi.org/10.1021/jp014452p.

(21) Zou, S.; Chan, H. Y. H.; Williams, C. T.; Weaver, M. J. Formation and Stability of Oxide Films on Platinum-Group Metals in Electrochemical and Related Environments As Probed by Surface-Enhanced Raman Spectroscopy:  Dependence on the Chemical Oxidant. *Langmuir* **2000**, *16* (2), 754–763. https://doi.org/10.1021/la990544i.

(22) Pavlovic, Z.; Ranjan, C.; Gastel, M. van; Schlögl, R. The Active Site for the Water Oxidising Anodic Iridium Oxide Probed through in Situ Raman Spectroscopy. *Chem. Commun.* **2017**, *53* (92), 12414–12417. https://doi.org/10.1039/C7CC05669A.

(23) Pavlovic, Z.; Ranjan, C.; Gao, Q.; van Gastel, M.; Schlögl, R. Probing the Structure of a Water-Oxidizing Anodic Iridium Oxide Catalyst Using Raman Spectroscopy. *ACS Catal.* **2016**, *6* (12), 8098–8105. https://doi.org/10.1021/acscatal.6b02343.

(24) H. Saeed, K.; Forster, M.; Li, J.-F.; J. Hardwick, L.; J. Cowan, A. Water Oxidation Intermediates on Iridium Oxide Electrodes Probed by in Situ Electrochemical SHINERS. *Chem. Commun.* **2020**, *56* (7), 1129–1132. https://doi.org/10.1039/C9CC08284K.

(25) Mom, R. V.; Falling, L. J.; Kasian, O.; Algara-Siller, G.; Teschner, D.; Crabtree, R. H.; Knop-Gericke, A.; Mayrhofer, K. J. J.; Velasco-Vélez, J.-J.; Jones, T. E. Operando Structure–Activity–Stability Relationship of Iridium Oxides during the Oxygen Evolution Reaction. *ACS Catal.* **2022**, *12* (9), 5174–5184. https://doi.org/10.1021/acscatal.1c05951.

(26) Frevel, L. J.; Mom, R.; Velasco-Vélez, J.-J.; Plodinec, M.; Knop-Gericke, A.; Schlögl, R.; Jones, T. E. In Situ X-Ray Spectroscopy of the Electrochemical Development of Iridium Nanoparticles in Confined Electrolyte. *J. Phys. Chem. C* **2019**, *123* (14), 9146–9152. https://doi.org/10.1021/acs.jpcc.9b00731.

(27) Velasco-Vélez, J. J.; Jones, T. E.; Streibel, V.; Hävecker, M.; Chuang, C.-H.; Frevel, L.; Plodinec, M.; Centeno, A.; Zurutuza, A.; Wang, R.; Arrigo, R.; Mom, R.; Hofmann, S.; Schlögl, R.; Knop-Gericke, A. Electrochemically Active Ir NPs on Graphene for OER in Acidic Aqueous Electrolyte Investigated by in Situ and Ex Situ Spectroscopies. *Surf. Sci.* **2019**, *681*, 1–8. https://doi.org/10.1016/j.susc.2018.10.021.

(28) Pfeifer, V.; Jones, T. E.; Vélez, J. J. V.; Arrigo, R.; Piccinin, S.; Hävecker, M.; Knop-Gericke, A.; Schlögl, R. In Situ Observation of Reactive Oxygen Species Forming on Oxygen-Evolving Iridium Surfaces. *Chem. Sci.* **2017**, *8* (3), 2143–2149. https://doi.org/10.1039/C6SC04622C.

(29) Abbott, D. F.; Lebedev, D.; Waltar, K.; Povia, M.; Nachtegaal, M.; Fabbri, E.; Copéret, C.; Schmidt, T. J. Iridium Oxide for the Oxygen Evolution Reaction: Correlation between Particle Size, Morphology, and the Surface Hydroxo Layer from Operando XAS. *Chem. Mater.* **2016**, *28* (18), 6591–6604. https://doi.org/10.1021/acs.chemmater.6b02625.

(30) Pedersen, A. F.; Escudero-Escribano, M.; Sebok, B.; Bodin, A.; Paoli, E.; Frydendal, R.; Friebel, D.; Stephens, I. E. L.; Rossmeisl, J.; Chorkendorff, I.; Nilsson, A. Operando XAS Study of the Surface Oxidation State on a Monolayer IrOx on RuOx and Ru Oxide Based Nanoparticles for Oxygen Evolution in Acidic Media. *J. Phys. Chem. B* **2018**, *122* (2), 878–887. https://doi.org/10.1021/acs.jpcb.7b06982.

(31) Dionigi, F.; Zeng, Z.; Sinev, I.; Merzdorf, T.; Deshpande, S.; Lopez, M. B.; Kunze, S.; Zegkinoglou, I.; Sarodnik, H.; Fan, D.; Bergmann, A.; Drnec, J.; Araujo, J. F. de; Gliech, M.; Teschner, D.; Zhu, J.; Li, W.-X.; Greeley, J.; Cuenya, B. R.; Strasser, P. In-Situ Structure and Catalytic Mechanism of NiFe and CoFe Layered Double Hydroxides during Oxygen Evolution. *Nat. Commun.* **2020**, *11* (1), 2522. https://doi.org/10.1038/s41467-020-16237-1.

(32) Binninger, T.; Fabbri, E.; Patru, A.; Garganourakis, M.; Han, J.; Abbott, D. F.; Sereda, O.; Kötz, R.; Menzel, A.; Nachtegaal, M.; Schmidt, T. J. Electrochemical Flow-Cell Setup for In Situ X-Ray Investigations. *J. Electrochem. Soc.* **2016**, *163* (10), H906. https://doi.org/10.1149/2.0201610jes.

(33) Schröder, J.; Pittkowski, R. K.; Martens, I.; Chattot, R.; Drnec, J.; Quinson, J.; Kirkensgaard, J. J. K.; Arenz, M. Tracking the Catalyst Layer Depth-Dependent Electrochemical Degradation of a Bimodal Pt/C Fuel Cell Catalyst: A Combined Operando Small- and Wide-Angle X-Ray Scattering Study. *ACS Catal.* **2022**, *12* (3), 2077–2085. https://doi.org/10.1021/acscatal.1c04365.

(34) Schröder, J.; Pittkowski, R. K.; Du, J.; Kirkensgaard, J. J. K.; Arenz, M. Investigating the Particle Growth in Bimodal Pt/C Catalysts by In-Situ Small-Angle X-Ray Scattering: Challenges in the Evaluation of Stress Test Protocol-Dependent Degradation Mechanisms. *J. Electrochem. Soc.* **2022**, *169* (10), 104504. https://doi.org/10.1149/1945-7111/ac99a5.

(35) Martens, I.; Chattot, R.; Drnec, J. Decoupling Catalyst Aggregation, Ripening, and Coalescence Processes inside Operating Fuel Cells. *J. Power Sources* **2022**, *521*, 230851. https://doi.org/10.1016/j.jpowsour.2021.230851.

(36) Juelsholt, M.; S. Anker, A.; Lindahl Christiansen, T.; Vogel Jørgensen, M. R.; Kantor, I.; Risskov Sørensen, D.; Ø. Jensen, K. M. Size-Induced Amorphous Structure in Tungsten Oxide Nanoparticles. *Nanoscale* **2021**, *13* (47), 20144–20156. https://doi.org/10.1039/D1NR05991B.

(37) Christiansen, T. L.; Cooper, S. R.; Jensen, K. M. Ø. There's No Place like Real-Space: Elucidating Size-Dependent Atomic Structure of Nanomaterials Using Pair Distribution Function Analysis. *Nanoscale Adv.* **2020**, *2* (6), 2234–2254. https://doi.org/10.1039/D0NA00120A.

(38) Bennett, T. D.; Cheetham, A. K. Amorphous Metal–Organic Frameworks. *Acc. Chem. Res.* **2014**, *47* (5), 1555–1562. https://doi.org/10.1021/ar5000314.

(39) L. Billinge, S. J.; G. Kanatzidis, M. Beyond Crystallography : The Study of Disorder, Nanocrystallinity and Crystallographically Challenged Materials with Pair Distribution Functions. *Chem. Commun.* **2004**, *0* (7), 749–760. https://doi.org/10.1039/B309577K.

(40) Yang, X.; S. Masadeh, A.; R. McBride, J.; S. Božin, E.; J. Rosenthal, S.; L. Billinge, S. J. Confirmation of Disordered Structure of Ultrasmall CdSe Nanoparticles from X-Ray Atomic Pair Distribution Function Analysis. *Phys. Chem. Chem. Phys.* **2013**, *15* (22), 8480–8486. https://doi.org/10.1039/C3CP00111C.

(41) Lindahl Christiansen, T.; Kjær, E. T. S.; Kovyakh, A.; Röderen, M. L.; Høj, M.; Vosch, T.; Jensen, K. M. Ø. Structure Analysis of Supported Disordered Molybdenum Oxides Using Pair Distribution Function

Analysis and Automated Cluster Modelling. *J. Appl. Crystallogr.* **2020**, *53* (1), 148–158. https://doi.org/10.1107/S1600576719016832.

(42) Billinge, S. J. L.; Levin, I. The Problem with Determining Atomic Structure at the Nanoscale. *Science* **2007**, *316* (5824), 561–565. https://doi.org/10.1126/science.1135080.

(43) Jensen, K. M. Ø.; Christensen, M.; Juhas, P.; Tyrsted, C.; Bøjesen, E. D.; Lock, N.; Billinge, S. J. L.; Iversen, B. B. Revealing the Mechanisms behind SnO2 Nanoparticle Formation and Growth during Hydrothermal Synthesis: An In Situ Total Scattering Study. *J. Am. Chem. Soc.* **2012**, *134* (15), 6785–6792. https://doi.org/10.1021/ja300978f.

(44) Young, C. A.; Goodwin, A. L. Applications of Pair Distribution Function Methods to Contemporary Problems in Materials Chemistry. *J. Mater. Chem.* **2011**, *21* (18), 6464–6476. https://doi.org/10.1039/C0JM04415F.

(45) Zhu, H.; Huang, Y.; Ren, J.; Zhang, B.; Ke, Y.; Jen, A. K.-Y.; Zhang, Q.; Wang, X.-L.; Liu, Q. Bridging Structural Inhomogeneity to Functionality: Pair Distribution Function Methods for Functional Materials Development. *Adv. Sci.* **2021**, *8* (6), 2003534. https://doi.org/10.1002/advs.202003534.

(46) Petkov, V.; Maswadeh, Y.; Lu, A.; Shan, S.; Kareem, H.; Zhao, Y.; Luo, J.; Zhong, C.-J.; Beyer, K.; Chapman, K. Evolution of Active Sites in Pt-Based Nanoalloy Catalysts for the Oxidation of Carbonaceous Species by Combined in Situ Infrared Spectroscopy and Total X-Ray Scattering. *ACS Appl. Mater. Interfaces* **2018**, *10* (13), 10870–10881. https://doi.org/10.1021/acsami.7b19574.

(47) Zimmerli, N. K.; Müller, C. R.; Abdala, P. M. Deciphering the Structure of Heterogeneous Catalysts across Scales Using Pair Distribution Function Analysis. *Trends Chem.* **2022**, *4* (9), 807–821. https://doi.org/10.1016/j.trechm.2022.06.006.

(48) Newton, M. A.; Chapman, K. W.; Thompsett, D.; Chupas, P. J. Chasing Changing Nanoparticles with Time-Resolved Pair Distribution Function Methods. *J. Am. Chem. Soc.* **2012**, *134* (11), 5036–5039. https://doi.org/10.1021/ja2114163.

(49) Shan, S.; Petkov, V.; Yang, L.; Luo, J.; Joseph, P.; Mayzel, D.; Prasai, B.; Wang, L.; Engelhard, M.; Zhong, C.-J. Atomic-Structural Synergy for Catalytic CO Oxidation over Palladium–Nickel Nanoalloys. *J. Am. Chem. Soc.* **2014**, *136* (19), 7140–7151. https://doi.org/10.1021/ja5026744.

(50) Mancini, A.; Barbieri, V. R.; Neuefeind, J. C.; Page, K.; Malavasi, L. Correlation between the Local Scale Structure and the Electrochemical Properties in Lithium Orthosilicate Cathode Materials. *J. Mater. Chem. A* **2014**, *2* (42), 17867–17874. https://doi.org/10.1039/C4TA04063E.

(51) Wiaderek, K. M.; Borkiewicz, O. J.; Castillo-Martínez, E.; Robert, R.; Pereira, N.; Amatucci, G. G.; Grey, C. P.; Chupas, P. J.; Chapman, K. W. Comprehensive Insights into the Structural and Chemical Changes in Mixed-Anion FeOF Electrodes by Using Operando PDF and NMR Spectroscopy. *J. Am. Chem. Soc.* **2013**, *135* (10), 4070–4078. https://doi.org/10.1021/ja400229v.

(52) Mathiesen, J. K.; Väli, R.; Härmas, M.; Lust, E.; Bülow, J. F. von; Jensen, K. M. Ø.; Norby, P. Following the In-Plane Disorder of Sodiated Hard Carbon through Operando Total Scattering. *J. Mater. Chem. A* **2019**, *7* (19), 11709–11717. https://doi.org/10.1039/C9TA02413A.

(53) Petkov, V.; Maswadeh, Y.; A. Vargas, J.; Shan, S.; Kareem, H.; Wu, Z.-P.; Luo, J.; Zhong, C.-J.; Shastri, S.; Kenesei, P. Deviations from Vegard's Law and Evolution of the Electrocatalytic Activity and Stability of Pt-Based Nanoalloys inside Fuel Cells by in Operando X-Ray Spectroscopy and Total Scattering. *Nanoscale* **2019**, *11* (12), 5512–5525. https://doi.org/10.1039/C9NR01069F.

(54) Wu, Z.-P.; Caracciolo, D. T.; Maswadeh, Y.; Wen, J.; Kong, Z.; Shan, S.; Vargas, J. A.; Yan, S.; Hopkins, E.; Park, K.; Sharma, A.; Ren, Y.; Petkov, V.; Wang, L.; Zhong, C.-J. Alloying–Realloying Enabled High Durability for Pt–Pd-3d-Transition Metal Nanoparticle Fuel Cell Catalysts. *Nat. Commun.* **2021**, *12* (1), 859. https://doi.org/10.1038/s41467-021-21017-6.

(55) Kong, Z.; Maswadeh, Y.; Vargas, J. A.; Shan, S.; Wu, Z.-P.; Kareem, H.; Leff, A. C.; Tran, D. T.; Chang, F.; Yan, S.; Nam, S.; Zhao, X.; Lee, J. M.; Luo, J.; Shastri, S.; Yu, G.; Petkov, V.; Zhong, C.-J. Origin of High Activity and Durability of Twisty Nanowire Alloy Catalysts under Oxygen Reduction and Fuel

15

Cell Operating Conditions. *J. Am. Chem. Soc.* **2020**, *142* (3), 1287–1299. https://doi.org/10.1021/jacs.9b10239.

(56) Bizzotto, F.; Quinson, J.; Zana, A.; Kirkensgaard, J. J. K.; Dworzak, A.; Oezaslan, M.; Arenz, M. Ir Nanoparticles with Ultrahigh Dispersion as Oxygen Evolution Reaction (OER) Catalysts: Synthesis and Activity Benchmarking. *Catal. Sci. Technol.* **2019**, *9* (22), 6345–6356. https://doi.org/10.1039/C9CY01728C.

(57) Quinson, J.; Neumann, S.; Wannmacher, T.; Kacenauskaite, L.; Inaba, M.; Bucher, J.; Bizzotto, F.; Simonsen, S. B.; Theil Kuhn, L.; Bujak, D.; Zana, A.; Arenz, M.; Kunz, S. Colloids for Catalysts: A Concept for the Preparation of Superior Catalysts of Industrial Relevance. *Angew. Chem.* **2018**, *130* (38), 12518–12521. https://doi.org/10.1002/ange.201807450.

(58) Bizzotto, F.; Quinson, J.; Schröder, J.; Zana, A.; Arenz, M. Surfactant-Free Colloidal Strategies for Highly Dispersed and Active Supported IrO2 Catalysts: Synthesis and Performance Evaluation for the Oxygen Evolution Reaction. *J. Catal.* **2021**, *401*, 54–62. https://doi.org/10.1016/j.jcat.2021.07.004.

(59) Martens, I.; Chattot, R.; Rasola, M.; Blanco, M. V.; Honkimäki, V.; Bizzotto, D.; Wilkinson, D. P.; Drnec, J. Probing the Dynamics of Platinum Surface Oxides in Fuel Cell Catalyst Layers Using in Situ X-Ray Diffraction. *ACS Appl. Energy Mater.* **2019**, *2* (11), 7772–7780. https://doi.org/10.1021/acsaem.9b00982.

(60) Marks, L. D. Experimental Studies of Small Particle Structures. *Rep. Prog. Phys.* **1994**, *57* (6), 603. https://doi.org/10.1088/0034-4885/57/6/002.

(61) Marks, L. D.; Smith, D. J. High Resolution Studies of Small Particles of Gold and Silver: I. Multiply-Twinned Particles. *J. Cryst. Growth* **1981**, *54* (3), 425–432. https://doi.org/10.1016/0022-0248(81)90494-2.

(62) Ino, S.; Ogawa, S. Multiply Twinned Particles at Earlier Stages of Gold Film Formation on Alkalihalide Crystals. *J. Phys. Soc. Jpn.* **1967**, *22* (6), 1365–1374. https://doi.org/10.1143/JPSJ.22.1365.

(63) Schmid, G. Clusters and Colloids: Bridges between Molecular and Condensed Material. *Endeavour* **1990**, *14* (4), 172–178. https://doi.org/10.1016/0160-9327(90)90040-X.

(64) Wakisaka, T.; Kusada, K.; Yamamoto, T.; Toriyama, T.; Matsumura, S.; Ibrahima, G.; Seo, O.; Kim, J.; Hiroi, S.; Sakata, O.; Kawaguchi, S.; Kubota, Y.; Kitagawa, H. Discovery of Face-Centred Cubic Os Nanoparticles. *Chem. Commun.* **2020**, *56* (3), 372–374. https://doi.org/10.1039/C9CC09192K.

(65) Masadeh, A. S.; Božin, E. S.; Farrow, C. L.; Paglia, G.; Juhas, P.; Billinge, S. J. L.; Karkamkar, A.; Kanatzidis, M. G. Quantitative Size-Dependent Structure and Strain Determination of CdSe Nanoparticles Using Atomic Pair Distribution Function Analysis. *Phys. Rev. B* **2007**, *76* (11), 115413. https://doi.org/10.1103/PhysRevB.76.115413.

(66) Jensen, K. M. Ø.; Juhas, P.; Tofanelli, M. A.; Heinecke, C. L.; Vaughan, G.; Ackerson, C. J.; Billinge, S. J. L. Polymorphism in Magic-Sized Au144(SR)60 Clusters. *Nat. Commun.* **2016**, *7* (1), 11859. https://doi.org/10.1038/ncomms11859.

(67) Page, K.; Hood, T. C.; Proffen, T.; Neder, R. B. Building and Refining Complete Nanoparticle Structures with Total Scattering Data. *J. Appl. Crystallogr.* **2011**, *44* (2), 327–336. https://doi.org/10.1107/S0021889811001968.

(68) Banerjee, S.; Liu, C.-H.; Lee, J. D.; Kovyakh, A.; Grasmik, V.; Prymak, O.; Koenigsmann, C.; Liu, H.; Wang, L.; Abeykoon, A. M. M.; Wong, S. S.; Epple, M.; Murray, C. B.; Billinge, S. J. L. Improved Models for Metallic Nanoparticle Cores from Atomic Pair Distribution Function (PDF) Analysis. *J. Phys. Chem. C* **2018**, *122* (51), 29498–29506. https://doi.org/10.1021/acs.jpcc.8b05897.

(69) Banerjee, S.; Liu, C.-H.; Jensen, K. M. Ø.; Juhás, P.; Lee, J. D.; Tofanelli, M.; Ackerson, C. J.; Murray, C. B.; Billinge, S. J. L. Cluster-Mining: An Approach for Determining Core Structures of Metallic Nanoparticles from Atomic Pair Distribution Function Data. *Acta Crystallogr. Sect. Found. Adv.* **2020**, *76* (1), 24–31. https://doi.org/10.1107/S2053273319013214.

(70) S. Kjær, E. T.; S. Anker, A.; N. Weng, M.; L. Billinge, S. J.; Selvan, R.; Ø. Jensen, K. M. DeepStruc: Towards Structure Solution from Pair Distribution Function Data Using Deep Generative Models. *Digit. Discov.* **2023**, *2* (1), 69–80. https://doi.org/10.1039/D2DD00086E.

(71) Anker, A. S.; Kj, E. T. S.; Dam, E. B.; Billinge, S. J. L.; Jensen, K. M. Ø.; Selvan, R. Characterising the Atomic Structure of Mono-Metallic Nanoparticles from x-Ray Scattering Data Using Conditional Generative Models. In *ML G2020*; San Diego, 2020.

(72) Geng, S.; Ji, Y.; Su, J.; Hu, Z.; Fang, M.; Wang, D.; Liu, S.; Li, L.; Li, Y.; Chen, J.-M.; Lee, J.-F.; Huang, X.; Shao, Q. Homogeneous Metastable Hexagonal Phase Iridium Enhances Hydrogen Evolution Catalysis. *Adv. Sci.* **2023**, *10* (11), 2206063. https://doi.org/10.1002/advs.202206063.

(73) Rogers, B.; Lehr, A.; Velázquez-Salazar, J. J.; Whetten, R.; Mendoza-Cruz, R.; Bazan-Diaz, L.; Bahena-Uribe, D.; José Yacaman, M. Decahedra and Icosahedra Everywhere: The Anomalous Crystallization of Au and Other Metals at the Nanoscale. *Cryst. Res. Technol.* **2023**, *58* (4), 2200259. https://doi.org/10.1002/crat.202200259.

(74) Mathiesen, J. K.; Quinson, J.; Blaseio, S.; Kjær, E. T. S.; Dworzak, A.; Cooper, S. R.; Pedersen, J. K.; Wang, B.; Bizzotto, F.; Schröder, J.; Kinnibrugh, T. L.; Simonsen, S. B.; Theil Kuhn, L.; Kirkensgaard, J. J. K.; Rossmeisl, J.; Oezaslan, M.; Arenz, M.; Jensen, K. M. Ø. Chemical Insights into the Formation of Colloidal Iridium Nanoparticles from In Situ X-Ray Total Scattering: Influence of Precursors and Cations on the Reaction Pathway. *J. Am. Chem. Soc.* **2023**, *145* (3), 1769–1782. https://doi.org/10.1021/jacs.2c10814.

(75) Willinger, E.; Massué, C.; Schlögl, R.; Willinger, M. G. Identifying Key Structural Features of IrOx Water Splitting Catalysts. *J. Am. Chem. Soc.* **2017**, *139* (34), 12093–12101. https://doi.org/10.1021/jacs.7b07079.

(76) Rogers, D. B.; Shannon, R. D.; Sleight, A. W.; Gillson, J. L. Crystal Chemistry of Metal Dioxides with Rutile-Related Structures. *Inorg. Chem.* **1969**, *8* (4), 841–849. https://doi.org/10.1021/ic50074a029.